IHBD. The SPACE technique facilitated high-resolution 3D MRC with excellent image quality at 3 T. These results, however, must be confirmed by further studies involving larger groups.

Conflict of interest

None.

References

[1] Vitellas KM, El-Dieb A, Vaswani KK, et al. MR cholangiopancreatography in patients with primary sclerosing cholangitis: interobserver variability and comparison with endoscopic retrograde cholangiopancreatography. Am J Roentgenol 2002;179:399–407.
[2] Aube C, Delorme B, Yzet T, et al. MR cholangiopancreatography versus endoscopic sonography in suspected common bile duct lithiasis: a prospective, comparative study. Am J Roentgenol 2005;184:55–62.
[3] Hoeffel C, Azizi L, Lewin M, et al. Normal and pathologic features of the postoperative biliary tract at 3D MR cholangiopancreatography and MR imaging. Radiographics 2006;26:1603–20.
[4] Watanabe Y, Nagayama M, Okumura A, et al. MR imaging of acute biliary disorders. Radiographics 2007;27:477–95.
[5] Masselli G, Gualdi G. Hilar cholangiocarcinoma: MRI/MRCP in staging and treatment planning. Abdom Imaging 2008;33:441–51.
[6] Limanond P, Raman SS, Ghobrial RM, Busuttil RW, Lu DS. The utility of MRCP in preoperative mapping of biliary anatomy in adult-to-adult living related liver transplant donors. J Magn Reson Imaging 2004;19:209–15.
[7] Merkle EM, Haugan PA, Thomas J, Jaffe TA, Gullotto C. 3.0- versus 1.5-T MR cholangiography: a pilot study. Am J Roentgenol 2006;186:516–21.
[8] Safar F, Kamura T, Okamuto K, Sasai K, Gejyo F. Magnetic resonance T1 gradient-echo imaging in hepatolithiasis. Abdom Imaging 2005;30:297–302.
[9] Lee VS, Morgan GR, Teperman LW, et al. MR imaging as the sole preoperative imaging modality for right hepatectomy: a prospective study of living adult-to-adult liver donor candidates. Am J Roentgenol 2001;176:1475–82.
[10] Limanond P, Raman SS, Ghobrial RM, Busuttil RW, Saab S, Lu DS. Preoperative imaging in adult-to-adult living related liver transplant donors: what surgeons want to know. J Comput Assist Tomogr 2004;28:149–57.
[11] Schick F. Whole-body MRI at high field: technical limits and clinical potential. Eur Radiol 2005;15:946–59.
[12] Merkle EM, Dale BM. Abdominal MRI at 3.0 T: the basics revisited. Am J Roentgenol 2006;186:1524–32.
[13] O'Regan DP, Fitzgerald J, Allsop J, et al. A comparison of MR cholangiopancreatography at 1.5 and 3.0 Tesla. Br J Radiol 2005;78:894–8.
[14] Isoda H, Kataoka M, Maetani Y, et al. MRCP imaging at 3.0 T vs. 1.5 T: preliminary experience in healthy volunteers. J Magn Reson Imaging 2007;25:1000–6.
[15] Lichy MP, Wietek BM, Mugler III JP, et al. Magnetic resonance imaging of the body trunk using a single-slab, 3-dimensional, T2-weighted turbo-spin-echo sequence with high sampling efficiency (SPACE) for high spatial resolution imaging: initial clinical experiences. Invest Radiol 2005;40:754–60.
[16] Weigel M, Hennig J. Contrast behavior and relaxation effects of conventional and hyperecho-turbo spin echo sequences at 1.5 and 3 T. Magn Reson Med 2006;55:826–35.
[17] Haystead CM, Dale BM, Merkle EM. N/2 ghosting artifacts: elimination at 3.0-T MR cholangiography with SPACE pulse sequence. Radiology 2008;246:589–95.
[18] Arizono S, Isoda H, Maetani YS, et al. High spatial resolution 3D MR cholangiography using high sampling efficiency technique (SPACE) at 3 T: comparison with conventional constant flip angle sequence in healthy volunteers. J Magn Reson Imaging 2008;28:685–90.
[19] Schindera ST, Miller CM, Ho LM, DeLong DM, Merkle EM. Magnetic resonance (MR) cholangiography: quantitative and qualitative comparison of 3.0 Tesla with 1.5 Tesla. Invest Radiol 2007;42:399–405.
[20] Barth MM, Smith MP, Pedrosa I, Lenkinski RE, Rofsky NM. Body MR imaging at 3.0 T: understanding the opportunities and challenges. Radiographics 2007;27:1445–64.
[21] Yeh BM, Breiman RS, Taouli B, Qayyum A, Roberts JP, Coakley FV. Biliary tract depiction in living potential liver donors: comparison of conventional MR, mangafodipir trisodium-enhanced excretory MR, and multi-detector row CT cholangiography—initial experience. Radiology 2004;230:645–51.
[22] Schroeder T, Malago M, Debatin JF, Goyen M, Nadalin S, Ruehm SG. All-in-one imaging protocols for the evaluation of potential living liver donors: comparison of magnetic resonance imaging and multidetector computed tomography. Liver Transpl 2005;11:776–87.
[23] Schroeder T, Radtke A, Kuehl H, Debatin JF, Malago M, Ruehm SG. Evaluation of living liver donors with an all-inclusive 3D multi-detector row CT protocol. Radiology 2006;238:900–10.

American Journal of Medical Genetics Part A 143A:3121–3126 (2007)

Visualization of Human Prenatal Development by Magnetic Resonance Imaging (MRI)

Kohei Shiota,[1,2]* Shigehito Yamada,[1] Tomoko Nakatsu-Komatsu,[1] Chigako Uwabe,[1] Katsumi Kose,[3] Yoshimasa Matsuda,[3] Tomoyuki Haishi,[4] Shinobu Mizuta,[5] and Tetsuya Matsuda[5]

[1]Congenital Anomaly Research Center, Kyoto University Graduate School of Medicine, Kyoto, Japan
[2]Department of Anatomy and Developmental Biology, Kyoto University Graduate School of Medicine, Kyoto, Japan
[3]Institute of Applied Physics, University of Tsukuba, Tsukuba, Japan
[4]MRTechnology, Inc., Tsukuba, Japan
[5]Graduate School of Informatics, Kyoto University, Kyoto, Japan

Received 4 July 2007; Accepted 16 July 2007

It is essential to visualize the structures of embryos and their internal organs three-dimensionally to analyze morphogenesis; this used to rely solely on serial histological sectioning and solid reconstruction, which were tedious and time-consuming. We have applied imaging with a magnetic resonance (MR) microscope equipped with a 2.35 T superconducting magnet to visualize human embryos; we were successful in acquiring high-resolution sectional images and in identifying the detailed structures of major organs. The imaging process was facilitated by using a super-parallel MR microscope. A dataset of MR images of more than 1,000 human embryos, now collected, will be important for future biomedical research and for education. © 2007 Wiley-Liss, Inc.

Key words: MR microscope; three-dimensional (3D) visualization; developmental imaging; human embryo

How to cite this article: Shiota K, Yamada S, Nakatsu-Komatsu T, Uwabe C, Kose K, Matsuda Y, Haishi T, Mizuta S, Matsuda T. 2007. Visualization of human prenatal development by magnetic resonance imaging (MRI). Am J Med Genet Part A 143A:3121–3126.

INTRODUCTION

Morphogenesis in the developing embryo takes place in three-dimensions, and the dimension of time is another important factor. Therefore, three-dimensional (3D) and four-dimensional (4D) visualization is essential to understand and analyze dynamic ontogenetic events. Traditionally, major methods of studying developmental anatomy relied on histological sectioning of embryos and solid reconstruction from serial sections to demonstrate the 3D structures of the embryonic body and organs. Well-known examples are the wax models of staged human embryos housed in the Carnegie Embryological Collection [Born, 1883; Heard, 1951, 1953, 1957]. Some of the historical reconstructed models are now preserved in the Human Developmental Anatomy Center in Washington, DC (http://nmhm.washingtondc.museum/collections/hdac/index.htm). Based on those reconstructed models, accurate drawings of human embryos were produced by skillful artists, such as James F. Didusch, who added invaluable information on human prenatal development [O'Rahilly, 1988]. However, such histological sectioning, solid reconstruction, and drawing are time-consuming and require special skills.

During the past 2–3 decades, computer-assisted reconstruction of biological structures has enabled the reconstruction of 3D embryos from serial histological sections with the aid of computer software. It has permitted reconstruction and manipulation of 3D images on the viewing screen. Recently, the Visible Embryo Project was carried out at the US National Museum of Health and Medicine (NMHM), utilizing the human embryo specimens of the Carnegie Col-

Tomoko Nakatsu-Komatsu's present address is Osaka Women's Junior College, Fujiidera, Osaka 583-8558, Japan.

Grant sponsor: Japanese Ministry of Education, Culture, Sports, Science and Technology; Grant number: 19390050; Grant sponsor: Japanese Ministry of Health, Labor and Welfare; Grant number: 17A-6; Grant sponsor: Japan Science and Technology Agency, BIRD Grant.

*Correspondence to: Kohei Shiota, M.D., Congenital Anomaly Research Center, Kyoto University Graduate School of Medicine, Kyoto 606-8501, Japan. E-mail: shiota@anat1.med.kyoto-u.ac.jp

DOI 10.1002/ajmg.a.31994

lection [Cohen, 2002]. Digitized 3D datasets of staged human embryos were completed and are now partly accessible on the web. After the Visible Human Project was discontinued in 2003, the Virtual Human Embryo Project was initiated (http://virtualhumanembryo.lsuhsc.edu/). The project consists of the Digitally Reproduced Embryonic Morphology (DREM) and Human Embryo Imaging and Reconstruction, Library OnLine Media (HEIRLOOM) components, containing high resolution microscopic morphology of human embryos and reconstructed 3D models, respectively. Such image datasets of human embryos are quite valuable, but the process still needs serially sectioned specimens and intensive labor to acquire the desirable precision and refinement of the images.

On the other hand, remarkable progress has been made in nondestructive imaging technologies in clinical medicine, such as computed tomography (CT) and magnetic resonance imaging (MRI). Smith [1999, 2000, 2001] and Smith et al. [1994, 1996, 1999], at Duke University, applied MRI to the visualization of embryos and were successful in obtaining MR images of embryos of both human and laboratory animals. MRI is a nondestructive technique, and efficiently provides 2D sectional images of embryos; 3D images of specimens can then be generated from the sectional data with the aid of computer software.

MRI is such a promising technique for developmental research, but initially, there were some problems and limitations in MRI of small embryos. One was the resolution of MR images, which was not high enough for visualizing fine structures in tiny embryos. To obtain sufficiently high resolution, we introduced a superconducting magnet (2.35 T) to MR microscopy, which significantly improved the quality of the MR images. Another problem was the speed of imaging. It usually takes several hours to image an embryo with MR, which is a serious limiting factor for imaging numerous specimens. This problem was overcome by inventing a super-parallel MR microscope, which enabled imaging of several specimens simultaneously and significantly reduced the time required [Matsuda et al., 2003]. In this article, we describe the "Kyoto Human Embryo Visualization Project," in which over 1,000 cases of staged human embryos are visualized by MR microscopy, and a database of developing human embryo images is established for future biomedical research.

MATERIALS AND METHODS

Embryo Specimens

The human embryo specimens in the Congenital Anomaly Research Center of Kyoto University were used for this study. The majority of the cases were obtained after therapeutic abortions given to healthy women during the first three months of pregnancy. The pregnancies were terminated mainly by dilatation and curettage, which enabled acquisition of undamaged, intact embryos. Further details of the embryo collection have been described in previous reports [Nishimura et al., 1968; Nishimura, 1975; Shiota, 1991; Yamada et al., 2006]. In the present study, approximately 1,400 specimens of externally normal human embryos at Carnegie stage (CS) 13 to CS23 were selected for MR microscopic imaging. The specimens were fixed in 4% formaldehyde or Bouin solution and stored in 4% formaldehyde.

MR Microscopic Imaging

Kose and his coworkers [Matsuda et al., 2003] developed a four-channel MR microscope with four unshielded gradient coil probes. The four-channel array probe was developed for a 2.35 T superconducting magnet. Each gradient coil probe consists of a rigid aluminum square frame [18 cm (W) × 20 cm (H) × 28 cm (D)] and slide planes made of thin brass plates (0.3 mm thick) acting as an RF shield. The RF coil units are exchangeable, and the diameter can be optimized for a given sample size. In the present study, 18 mm diameter four-turn solenoid coils were used for the 100 MHz signal excitation and detection frequency. The pulse sequence was a T_1-weighted 3D gradient echo sequence (TR = 100 ms, TE = 8 ms). Embryo specimens were imaged in test tubes (ID = 13.5 mm) filled with 4% formaldehyde solution. Further details of the MR microscope and its specifications have been described by Matsuda et al. [2003].

RESULTS

Figure 1 shows the 2D cross-sectional images of four fixed human embryos (CS22) selected from simultaneously acquired 3D datasets. The pulse sequence was a T_1-weighted conventional 3D spin-echo sequence (TR = 100 ms, TE = 8ms) and the image matrix size was 128 × 128 × 256. The resolution of these images is 120 μm^3. The images had a similar SNR value and no interference was observed between images acquired simultaneously.

In order to optimize the image contrast, we acquired T_1-weighted images using various repetition times (80–300 ms) and found that the 100 ms repetition gives the best image contrast for staged human embryos (data not shown).

Figure 2 shows that the MR image acquired as above enables identification of the structures in the major organs of human embryos in as much detail as the images of low-magnification histological sections (100× or lower magnification). Thus, it may be possible to identify major structural abnormalities in the embryo by MR microscopy, if there are any.

In Figure 3, 2D sectional images are shown for human embryos at CS18, CS20, and CS22. These

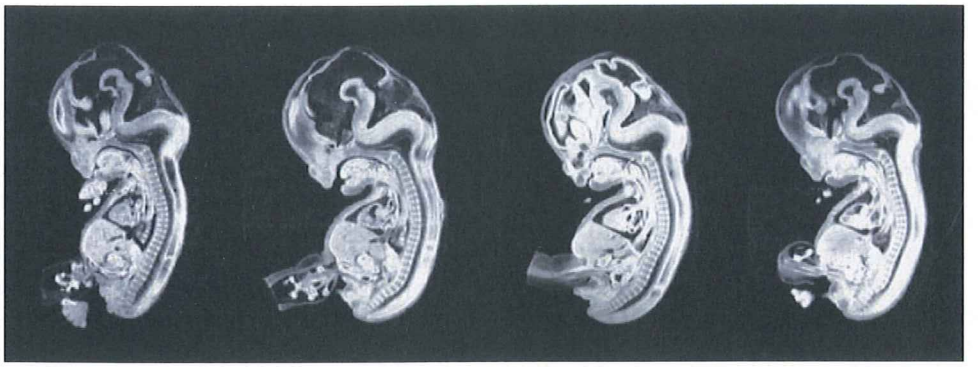

FIG. 1. Sectional images of four human embryo specimens (CS22) acquired simultaneously with the four-channel system of the super-parallel MR microscope. TR/TE = 100 ms/8 ms, spatial resolution = 120 μm^3, image matrix size = 128 × 128 × 256.

sectional MR images again demonstrate major anatomical structures in the embryo, even in those smaller than 20 mm in length.

Using sectional MR images, it is possible to generate the 3D images of each specimen. Figure 4 shows sectional MR images and 3D images of an embryo and its neural tube reconstructed using amira® software (Template Graphics Software, Inc.). The reconstructed images can be rotated on the viewing screen and cut in any desired plane to observe internal structures. Furthermore, 3D images of developing human embryos can be generated and the sequential morphogenetic process can be demonstrated with the aid of a computer graphics technique [Yamada et al., 2006].

DISCUSSION

By using a 2.35 T MR microscope, we acquired sectional 2D images of human embryos; the resolution was equivalent to that of low-magnification histological sections. One of the serious problems in MR imaging is the slow processing speed, and it usually takes several hours to obtain a 3D MR microscopic image dataset at a spatial resolution of a few to several tens of a micrometer [Johnson et al., 1993]. Kose and his coworkers [Matsuda et al., 2003] developed a super-parallel MR microscope, which enabled imaging of 4–8 samples simultaneously, significantly facilitating the speed of image processing. By using the novel super-parallel MR microscope, we could image over 1,000 human embryo specimens in a relatively short period of time (approximately 1 year).

MR imaging is nondestructive and does not need sectioning of embryonic tissues. MR imaging was applied to the embryos of the human and laboratory animals by the pioneering work of Smith [1999, 2000, 2001] and Smith et al. [1994, 1996, 1999]. More recently, Dhenain et al. [2001] applied spin-echo MRI techniques to fixed mouse embryos and identified the structures of the major organs in the embryo. Furthermore, Schneider and his coworkers [Schneider et al., 2003a,b; Schneider and Bhattacharya, 2004] used a

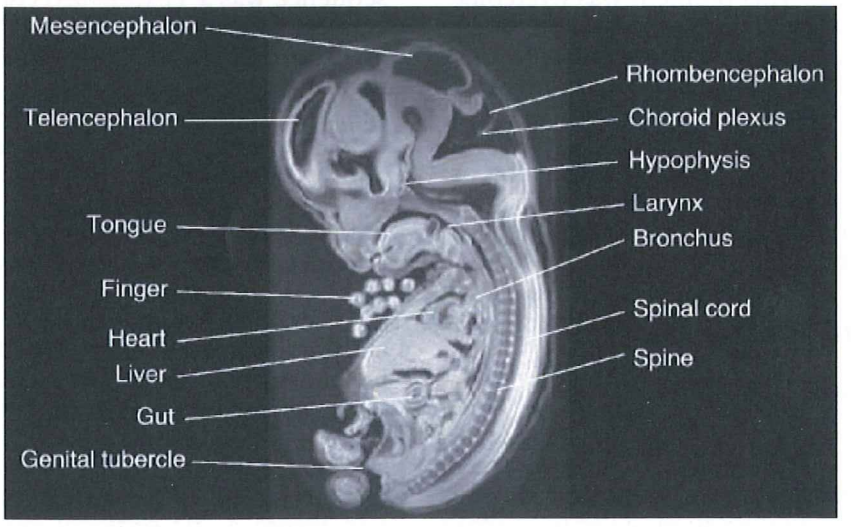

FIG. 2. MR image of a human embryo (CS23) in which structures of the major internal organs are identifiable.

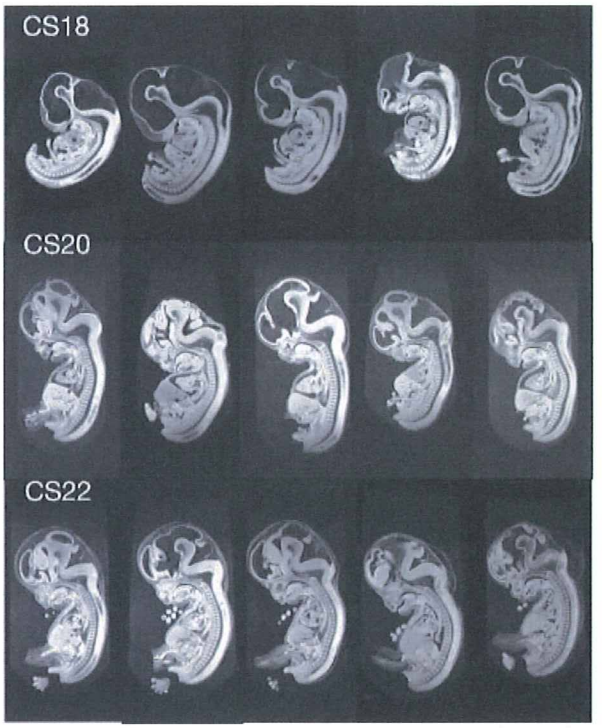

FIG. 3. 2D sectional images of human embryos at CS18, 20, and 22 selected from the datasets of staged human embryos.

T_1-weighted, fast gradient echo MR imaging technique and succeeded in identifying cardiac and other visceral malformations in mutant mouse embryos. By MRI, they visualized normal cardiac structures such as atria and ventricles, atrial and ventricular septa, valves, and great vessels in mouse fetuses as well as various cardiac anomalies, including atrial and ventricular septal defects, outflow tract defects, and malformations of the great vessels in mutant mice. Therefore, it is feasible to apply MR microscopic imaging to fast and efficient screening of embryos in genetic and teratological studies. In addition, if MR microscopy is used for examination of human abortuses, it would help identify internal visceral anomalies quickly, efficiently, and without dissection.

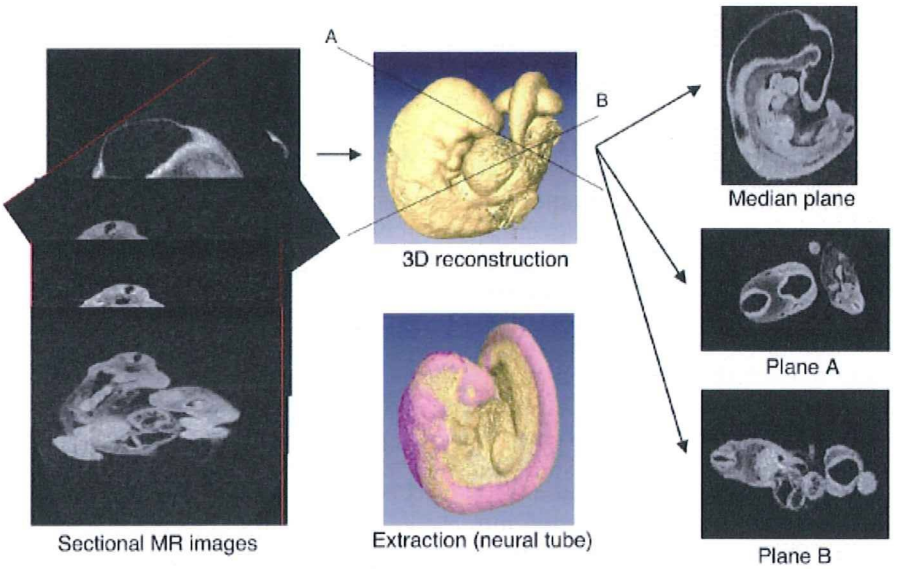

FIG. 4. 3D images of a human embryo and its neural tube (center) reconstructed from sectional MR data (amira® 3.1) and its sectional MR images (left). Sectional images at desired planes can also be generated (right). [Color figure can be viewed in the online issue, which is available at www.interscience.wiley.com.]

Thanks to the recent advancement in MRI technology, the resolution of images has been remarkably improved. In our study, the resolution now approaches 80 μm, and it is possible to identify various embryonic structures, such as the brain (and cerebral cortex), eyes, inner ears, pituitary gland, bronchi, lungs, stomach and intestines, kidneys, gonads, liver and spleen in embryos that are less than 30 mm in length (Fig. 2). We are now visualizing the internal organs of human embryos with external malformations to identify any internal abnormalities that may be present. MRI is nondestructive and does not need sectioning of specimens, which not only saves time and labor, but also allows precious specimens to remain intact. MRI can be complemented with other imaging techniques, such as micro-CT [Shibata and Nagano, 1996], optical projection tomography (OPT) [Sharpe et al., 2002; Sharpe, 2004], and episcopic fluorescence image capture (EFIC) [Weninger et al., 1998; Weninger and Mohun, 2002; Rosenthal et al., 2004] to visualize the detailed 3D and 4D structures in the embryo, and could be used in developmental and teratological research.

Another disadvantage of MRI is its high cost. However, some compact MR apparatuses are available at relatively reasonable cost [Haishi et al., 2001], and the cost of the apparatus might be compensated because MR enables imaging samples continuously, even at night. A super-parallel MR microscope can image four to eight samples simultaneously and contribute to the reduction in cost, as well.

In the "post-sequence" era, it is becoming important to unravel the functions of genes and their interactions in the organism, which cannot be elucidated by conventional molecular biological techniques. To this end, it is necessary to visualize gene expression patterns in the embryo and analyze the 3D and 4D localization of multiple genes in various tissues. The data of gene expression in the embryo obtained by in situ hybridization in single-sections and whole-mount samples can be mapped in 3D images of the embryo, and their dynamic expression patterns can be analyzed. Such databases of dynamic gene expression would help unravel the yet unknown functions, pathways, and interaction of multiple genes in normal and abnormal development. Some 3D databases of developmental gene expression are being furnished for mouse embryos by groups at the University of Edinburgh and MRC [EMAP and EMAGE; Baldock et al., 2003], at the University of Vienna [GeneEMAC; Streicher et al., 2000], and at the Jackson Laboratory [GXD; Smith et al., 2007]. It is hoped that a similar database for human embryos will enable the comparison of developmental gene expression patterns in human and laboratory animals, and provide a clue to identifying new gene functions in the human embryo, as well as gene mutations responsible for human birth defects.

Sequential 3D images of human embryos also have the potential to serve as a reference and an important data resource for human developmental studies similar to the Visible Human Database that contains digitized serial cross-sectional images of normal male and female adult bodies [Ackerman, 1998, 1999] (http://www.nlm.nih.gov/research/visible/visible_human.html). They could serve as models of network-accessible digital image libraries for medical research and education. Actually, various new research projects have emerged from the Visible Human Project, such as the invention of internet-enabled visualization tools and navigation technologies for anatomy education and research; establishing comprehensive atlases of the human body for clinical imaging diagnosis; and virtual reality and surgical simulation for health care education and training [Ackerman et al., 2001]. Similarly, 3D visualization of human embryonic development should be useful in biomedical research and education because such images and movie-illustration of sequential developmental changes would help researchers and students understand the dynamic morphogenetic movements visually that occur in three- and four-dimensions.

ACKNOWLEDGMENTS

The contribution of collaborating obstetricians who provided us with human embryo specimens is gratefully acknowledged. We thank Dr. Mikiko Kobayashi-Miura for generating 3D reconstructed images of embryos. This work was supported by grants of the Japanese Ministry of Education, Culture, Sports, Science and Technology (Grant number 19390050) and the Japanese Ministry of Health, Labor and Welfare (Grant number: 17A-6) and by the BIRD grant of the Japan Science and Technology Agency.

REFERENCES

Ackerman MJ. 1998. The visible human project: A resource for anatomical visualization. Medinfo 9:1030–1032.

Ackerman MJ. 1999. The visible human project: A resource for education. Acad Med 74:667–670.

Ackerman MJ, Yoo T, Jenkins D. 2001. From data to knowledge—The visible human project continues. Medinfo 10:887–890.

Baldock RA, Bard JB, Burger A, Burton N, Christiansen J, Feng G, Hill B, Houghton D, Kaufman M, Rao J, Sharpe J, Ross A, Stevenson P, Venkataraman S, Waterhouse A, Yang Y, Davidson DR. 2003. EMAP and EMAGE: A framework for understanding spatially organized data. Neuroinformatics 1: 309–325.

Born G. 1883. Die Plattenmodelliermethode. Arch Mikr Anat 22:584–599.

Cohen J. 2002. Embryo development at the click of a mouse (News of the week). Science 297:1629.

Dhenain M, Ruffins SW, Jacobs RE. 2001. Three-dimensional digital mouse atlas using high-resolution MRI. Dev Biol 232: 458–470.

Haishi T, Uematsu T, Matsuda Y, Kose K. 2001. Development of a 1.0 T MR microscope using a Nd-Fe-B permanent magnet. Magn Reson Imaging 19:875–880.

Heard OO. 1951. Section compression photographically rectified. Anat Rec 109:745–755.

Heard OO. 1953. The influence of surface forces in microtomy. Anat Rec 117:725–739.

Heard OO. 1957. Methods used by C.H. Heuser in preparing and sectioning early embryos. Contrib Embryol Carnegie Inst 36:1–18.

Johnson GA, Benveniste H, Black RD, Hedlund LW, Maronpot RR, Smith BR. 1993. Histology by magnetic resonance microscopy. Magn Reson Q 9:1–30.

Matsuda Y, Utsuzawa S, Kurimoto T, Haishi T, Yamazaki Y, Kose K, Anno I, Marutani M. 2003. Super-parallel MR microscope. Magn Reson Med 50:183–189.

Nishimura H. 1975. Prenatal versus postnatal malformations based on the Japanese experience on induced abortions in the human being. In: Blandau RJ, editor. Aging gametes. Basel: S. Karger AG. p 349–368.

Nishimura H, Takano K, Tanimura T, Yasuda M. 1968. Normal and abnormal development of human embryos: First report of the analysis of 1,213 intact embryos. Teratology 1:281– 290.

O'Rahilly R. 1988. One hundred years of human embryology. In: Kalter H, editor. Issues and reviews in teratology, Vol. 4. New York: Plenum Press. p 81–128.

Rosenthal J, Mangal V, Walker D, Bennett M, Mohun TJ, Lo CW. 2004. Rapid high resolution three dimensional reconstruction of embryos with episcopic fluorescence image capture. Birth Defects Res Pt C Embryo Today 72:213–223.

Schneider JE, Bhattacharya S. 2004. Making the mouse embryo transparent: Identifying developmental malformations using magnetic resonance imaging. Birth Defects Res (Part C) Embryo Today 72:241–249.

Schneider JE, Bamforth SD, Farthing CR, Clarke K, Neubauer S, Bhattacharya S. 2003. High-resolution imaging of normal anatomy, and neural and adrenal malformations in mouse embryos using magnetic resonance microscopy. J Anat 202: 239–247.

Schneider JE, Bamforth SD, Farthing CR, Clarke K, Neubauer S, Bhattacharya S. 2003. Rapid identification and 3D reconstruction of complex cardiac malformations in transgenic mouse embryos using fast gradient echo sequence magnetic resonance imaging. J Mol Cell Cardiol 35:217–222.

Sharpe J. 2004. Optical projection tomography. Annu Rev Biomed Eng 6:209–228.

Sharpe J, Ahlgren U, Perry P, Hill B, Ross A, Hecksher-Sorensen J, Baldock R, Davidson D. 2002. Optical projection tomography as a tool for 3D microscopy and gene expression studies. Science 296:541–545.

Shibata T, Nagano T. 1996. Applying very high resolution microfocus X-ray CT and 3-D reconstruction to the human auditory apparatus. Nat Med 2:933–935.

Shiota K. 1991. Development and intrauterine fate of normal and abnormal human conceptuses. Congenit Anom Kyoto 31: 67–80.

Smith BR. 1999. Visualizing human embryos. Sci Am 280:76–81.

Smith BR. 2000. Magnetic resonance imaging analysis of embryos. In: Tuan R, Lo CW, editors. Developmental biology protocols. Totawa, NJ: Humana Press Inc. p 211–216.

Smith BR. 2001. Magnetic resonance microscopy in cardiac development. Microsc Res Technol 52:323–330.

Smith BR, Johnson GA, Groman EV, Linney E. 1994. Magnetic resonance microscopy of mouse embryos. Proc Natl Acad Sci USA 91:3530–3533.

Smith BR, Linney E, Huff DS, Johnson GA. 1996. Magnetic resonance microscopy of embryos. Comput Med Imaging Graph 20:483–490.

Smith BR, Huff DS, Johnson GA. 1999. Magnetic resonance imaging of embryos: An Internet resource for the study of embryonic development. Comput Med Imaging Graph 23: 33–40.

Smith CM, Finger JH, Hayamizu TF, McCright IJ, Eppig JT, Kadin JA, Richardson JE, Ringwald M. 2007. The mouse Gene Expression Database (GXD): 2007 update. Nucleic Acids Res 35:D618–D623 (Database issue).

Streicher J, Donat MA, Strauss B, Sporle R, Schughart K, Muller GB. 2000. Computer-based three-dimensional visualization of developmental gene expression. Nat Genet 25:147–152.

Weninger WJ, Mohun T. 2002. Phenotyping transgenic embryos: A rapid 3-D screening method based on episcopic fluorescence image capturing. Nat Genet 30:59–65.

Weninger WJ, Meng S, Streicher J, Müller GB. 1998. A new episcopic method for rapid 3-D reconstruction: Applications in anatomy and embryology. Anat Embryol (Berl) 197:341–348.

Yamada S, Uwabe C, Nakatsu-Komatsu T, Minekura Y, Iwakura M, Motoki T, Nishimiya K, Iiyama M, Kakusho K, Minoh M, Mizuta S, Matsuda T, Matsuda Y, Haishi T, Kose K, Fujii S, Shiota K. 2006. Graphic and movie illustrations of human prenatal development and their application to embryological education based on the human embryo specimens in the Kyoto Collection. Dev Dyn 235:468–477.

A Model for Simulation of Infant Cardiovascular Response to Orthostatic Stress

Yutaka Nobuaki[1], Akira Amano[1], Takao Shimayoshi[2], Jianyin Lu[3], Eun B. Shim[4], and Tetsuya Matsuda[1]

[1] Graduate School of Informatics, Kyoto University, Kyoto, Japan
{amano,nobuaki,tetsu}@i.kyoto-u.ac.jp
[2] ASTEM Research Institute of Kyoto, Kyoto, Japan
simayosi@astem.or.jp
[3] Cell/Biodynamics Simulation Project, Kyoto University, Kyoto, Japan
lu@biosim.med.kyoto-u.ac.jp
[4] Division of Mechanical & Biomedical Engineering, Kangwon National University, Korea
ebshim@kangwon.ac.kr

Abstract. We developed an infant circulation model which incorporates an accurate myocardial cell model including a beta adrenergic system. The beta adrenergic system is essential for the response reproduction of the baroreflex control system. The proposed model was constructed by modifying the parameters of a human adult circulation model with the aid of a guinea pig myocardial cell model, whose baseline heart rate is close to that of an infant. The presented model is in good agreement with results obtained in physiological experiments.

1 Introduction

To improve our knowledge on biological mechanisms, quantitative and integrative studies of each biological element are necessary. Despite the rapid advancement in the accumulation of quantitative data from biological elements, the integrated systems are still not well analyzed. The simulation of complex biological models is of great importance, due to its potency in the analysis of biological functions. Biosimulation models are also expected to develop into powerful tools for medical education.

As a consequence of their complex physiology obstetric patients, neonates, and children often require rapid therapeutic intervention in the acute phase. We believe that simulation models for these patients will be of significant use in medical training. Since the cardiovascular system is one of the most essential physiological systems, we focused on constructing a baseline cardiovascular simulation model for infants.

Goodwin et al. [1] presented an infant cardiovascular simulation model which consists of four heart chambers and 6 compartments. The model also integrates an autonomous nervous system, however, the heart chamber model is based on

F.B. Sachse and G. Seemann (Eds.): FIMH 2007, LNCS 4466, pp. 190–199, 2007.

a time varying elastance model, for which the evaluation of the effects on electrophysiological aspects of the myocardial cells is difficult. Since the myocardial cell models are becoming increasingly accurate[2], incorporation of the same into cardiovascular models is unquestionably desirable.

In this paper, we propose an infant cardiovascular model which incorporates such an accurate myocardial cell model.

2 Cardiovascular Model

Since our model considers an autonomous nervous system, we used a myocardial cell model which includes a beta adrenergic stimulus system. The model is constructed from elementary models decribed in this section(Table1).

Table 1. Elementary models of proposed infant cardiovascular model

Element	Model	Species	Reference
cardiac cell	Kyoto model	guinea pig	[3]
left ventricle	Laplace law		
circulation	Heldt model	adult human	[4]
control system	Heldt model	adult human	[4]

2.1 Myocardial Cell and Left Ventricle Model

The Kyoto model proposed by Noma et al was used for the myocardial cell model. The Kyoto model is an accurate cell model which incorporates most of the known ion channels and transporters, a mitochondria as well as a contraction model. In addition, it is the only model which incorporates a beta adrenergic system. The contractility of the model is modified by the isoproterenol (ISP) concentration (Fig.1). Note that the Kyoto model shows a decrease in maximum force and increase of minimum force when the heart rate increase (Fig.2).

For the left ventricle model the Laplace law was applied. Denoting the wall thickness with h, the radius with R, the LV pressure with P_{lv} and the myocardial cell force by F_{ext}, the Laplace law is represented as $2F_{ext}/R = P_{lv}/h$ [5]. Through this equation, LV pressure and volume are related to the cell contraction force.

2.2 Circulation Model

In clinical tests, the head up tilt (HUT) is commonly used for both, adults and infants, to verify the response of the baroreflex system. Likewise, in our study, HUT was used to test the baroreflex. Accordingly, the circulation model was considered to have several compartments, which account for posture change. The human adult circulation model proposed by Heldt et al. [4] is

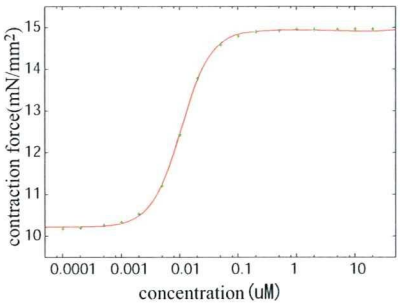

Fig. 1. Relation between ISP concentration and maximum contraction force

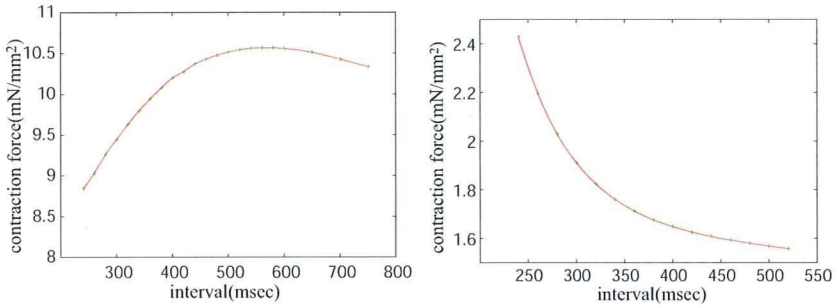

(a) Maximum force (b) Minimum force

Fig. 2. Relation between RR interval and force

mathematically formulated in terms of an electric analogous model with 12 compartments that can represent the posture change (Fig.3). 10 compartments representing the peripheral circulation show linear resistance (R) and capacitance (C). The legs, splanchnic and abdominal venous compartments exhibit nonlinear pressure-volume relations according to the following equation,

$$\Delta V = \frac{2 \cdot \Delta V_{max}}{\pi} \cdot \arctan\left(\frac{\pi \cdot C_0}{2 \cdot \Delta V_{max}} \cdot \Delta P_{trans}\right). \tag{1}$$

ΔV represents the compartment volume change due to change in transmural pressure ΔP_{trans}. ΔV_{max} represents the maximal change in compartment volume and C_0 the compartment compliance at baseline transmural pressure. An additional control system built into the model maintains the blood pressure which controls heart rate (HR), peripheral resistance (R), venous zero-pressure filling volume (V^0) and heart contractility (C_{sys}) [4].

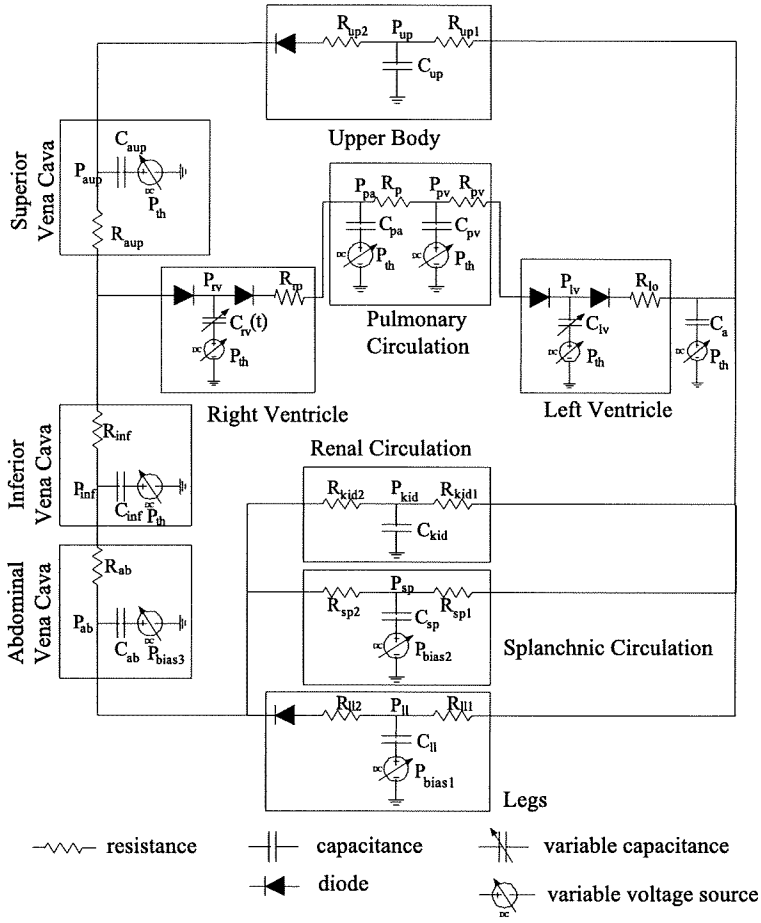

Fig. 3. Heldt circulation model. [4]

3 Construction of Infant Circulation Model

Since the species and the age of the subjects each model is based on is different from that of the human infant, we modified the parameters and the structure of each model.

3.1 Circulation Model Scaling

Since the baseline heart rate of infants is around 130–150(bpm), the myocardial model was constructed by means of the Kyoto model at a baseline heart rate of 150(bpm). The only modification to the model was multiplication of the cross-bridge sliding rate by 7.0, since the original value was determined for 25 degrees room temperature, while the temperature of an infant is around 37 degrees.

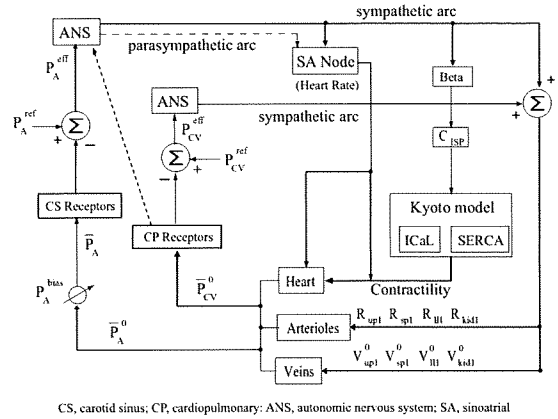

Fig. 4. Block diagram of control system

For the circulation model, we modified the hemodynamic parameters of the Heldt model to fit the infant circulation parameters. Thereby, a scaling method proposed by Goodwin et al. [1] was employed. In their study, the adult human circulation model proposed by Beneken et al. [6] was adjusted to the circulation of a 6 month old infant. Each resistance parameter is multiplied by 2.0, the compliance parameter by 1/5.43 and zero-pressure filling volume by 0.13. The same scaling factors were adopted for our model.

We used the Heldt model initial compartment pressures as initial compartment pressures. From these pressure values, the initial compartment volumes can be calculated, leading to the initial total blood volume of 783.5ml which is slightly large compared to the physiological value of 640ml.

3.2 Control Model Modification

In the Heldt model, the heart function is controlled by its contractility and the given heart rate. We took over the same control system without any parameter modifications. However, in the Heldt model, heart contractility is controlled by the maximum elastance parameter of their time varying elastance model, while the contractility in our heart model is controlled by the ISP concentration. Thus, the control system was modified to influence the ISP concentration. Additionally, in the Heldt model, heart contractility is controlled independently from the heart rate, which is in opposition to the real myocardial cell as well as the myocardial cell model applied in our study. Consequently, deriving a transform function between original heart contractility control signal and ISP concentration was the first task.

An open loop control system was created using the original Heldt model and the pressure input to the baroreceptor varied.In this way, the relation between the heart contractility control signal and the mean blood pressure was determined. Subsequently an open loop control system using the Heldt model was

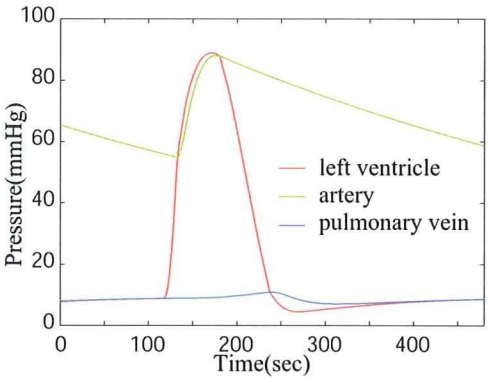

Fig. 5. Pressure at left ventricle, artery and pulmonary vein in resting situation in supine position

designed incorporating our Laplace heart model and the cell model. By changing the ISP concentration, the relation between the ISP concentration and mean blood pressure was deduced. By deleting the mean blood pressure parameter from these two functions, we obtained the desired transform function from heart contractility control signal to ISP concentration.

Subsequently, a compensation function for the heart contractility which is modified with the heart rate was derived. In the real cell, the relation between the cell force and heart rate changes nonlinearly according to the ISP concentration. However, in our model this relation is assumed to be independent of the ISP concentration. The block diagram of our control system is shown in Fig.4.

4 Experimental Results

4.1 Resting Hemodynamics

Figure 5 shows the resulting pressure at the left ventricle, artery and pulmonary vein in resting situation in supine position. Table 2 demonstrates that the hemodynamic parameters of the simulation results match the physiological values from [7][8][9].

4.2 HUT Test

Using the completed model a simulation experiment of the HUT test was conducted. To simulate the tilt effect, we applied following bias pressure to the lower three compartments in accordance with [4].

$$P_{bias} = \begin{cases} P_{max} \cdot \sin(\alpha(t)) & t_0 \leq t \leq t_0 + t_{tilt} \\ P_{max} \cdot \sin(\alpha_{max}) & t > t_0 + t_{tilt} \end{cases} \quad (2)$$

Table 2. Hemodynamic parameters in the supine position at rest

Variable	Target	Simulation results
Heart		
HR(bpm)	115-145	150
LVEDV(ml)	17	27.1
LVEDP(mmHg)	5	6.08
LVESV(ml)	5	13.4
LVESP(mmHg)	82	88.0
CO(L/min)	1.2-2.0	2.0
Circulation		
maxAP(mmHg)	70-110	87.1
minAP(mmHg)	50-65	54.3
CVP(mmHg)	3-12	1.8-3.2

HR: Heart rate, LVEDV: left ventricular end-diastolic volume, LVEDP: left ventricular end-diastolic pressure, LVESV: left ventricular end-systolic volume, LVESP: left ventricular end-systolic pressure, CO: cardiac output, maxAP: maximum arterial pressure, minAP: minimum arterial pressure, CVP: central venous pressure.

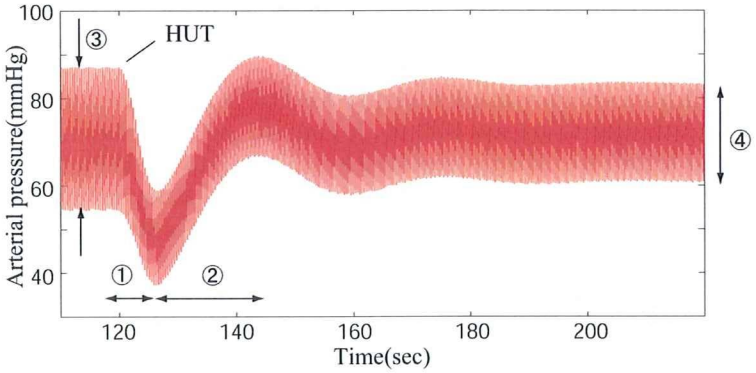

Fig. 6. Arterial pressure at HUT test

Here, t_0 and t_{tilt} denote starting and ending time of the tilt, α_{max} denotes the final angle of the tilt and P_{max} the maximum bias. We used 40.0, 7.0, 5.0 for the P_{max} of the renal, splanchnic and legs compartment, respectively.

In the physiological experiment with a human adult, the blood volume decreases by 600ml within 35 minutes [10]. This fact is modeled in the Heldt model as follows:

$$V_{total} = (5700ml - \Delta V) + \Delta V \cdot 0.9^{\frac{t-t_0}{60s}} \tag{3}$$

$$\Delta V = 600ml \cdot \sin(\alpha_{max}) \tag{4}$$

Table 3. Comparison of transient response to HUT test with experimental data

Variables	Unit	Simulation	experiments
(1)	s	6.3	2—9
(2)	s	17.6	4—30
(3)	mmHg	32.7	22
(4)	mmHg	23.2	17
(5)	beats/min	150	132
(6)	beats/min	169	150

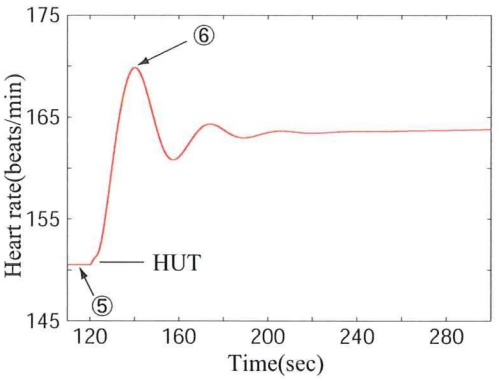

Fig. 7. Heart rate at HUT test

In our model, we modified the above equation to fit the total volume.

$$V_{total} = (783.9ml - \Delta V) + \Delta V \cdot 0.9^{\frac{t-t_0}{60s}} \tag{5}$$

$$\Delta V = 78ml \cdot \sin(\alpha_{max}) \tag{6}$$

In the simulation, the tilt angle was increased from 0 to 70 degree in 2 seconds. The tilt starting time was at 120 seconds. The resulting arterial pressure, heart rate are shown in Fig.6, Fig.7. The resulting features of the hemodynamics are shown in Table 3 in comparison with results gained in physiological experiments. The results are in good agreement with the experimental data.

5 Discussion

By means of the experimental results presented in section 4.1, we have verified that our simulation model is suitable to reproduce the physiological values of infant hemodynamics.

The simulation experiments explained in section 4.2, showed good agreement with experimental data published by Moss et al. [11](Fig.8). They reported that the pressure decreases within 2 to 9 seconds after the start of HUT, and recovers

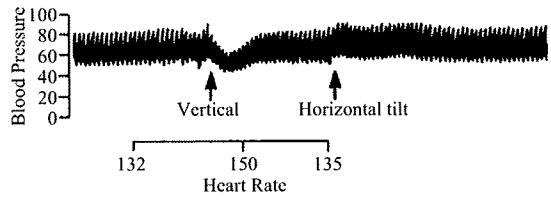

Fig. 8. Blood pressure of HUT test by Moss et al. [11]

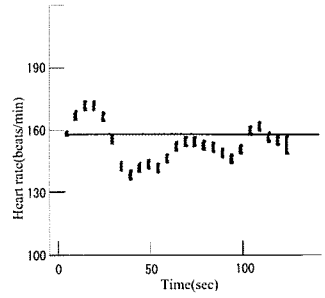

Fig. 9. Heart rate of HUT test by Edner et al. [12]

within 4 to 30 seconds. The pressure pulse width changes from 22 mmHg to 17 mmHg, which equals a 23% decrease. Further, they reported that the heart rate increases from 8 to 38 bpm which equals an 14% increase. Our simulation result showed 29% decrease of the pressure pulse width and 14% increase of heart rate, which is significantly close to the experimental data stated above.

Edner et al. reported the heart rate change when using a 45 degree HUT test [12](Fig.9). Their experimental results showed that the heart rate initially increases, but then decreases again and finally recovers. Also in this case, our simulation results were in good agreement with the experimental results.

From the above, we conclude that our circulation model and control model is capable to simulate the infant hemodynamics not only at resting position but also its response in a HUT test.

6 Conclusions

We developed an infant circulation model which incorporates an accurate myocardial cell model including a beta adrenergic system. The beta adrenergic system is essential in order to reproduce the response of the baroreflex control system. Our model showed good agreement with the physiological experiments. This model may be used to demonstrate the essential functions of the infant cardiovascular dynamics. Especially in clinical and medical training this could be a valuable tool.

Acknowledgement

The authors would like to express sincere thanks to Dr. Y. Shimizu, Kyoto Univ., for English proofreading. This work was supported by the Leading Project for Biosimulation, MEXT.

References

1. Goodwin, J.A., van Meurs, W.L., Sa Couto, C.D., Beneken, J.E.W., Graves, S.A.: A Model for Educational Simulation of Infant Cardiovascular Physiology. International Anesthesia Research Society 99, 1655 (2004)
2. Faber, G., Rudy, Y.: Action Potential and Contractility Changes in [Na+]i Overloaded Cardiac Myocytes: A Simulation Study. Biophys J. 78(5), 2392–2404 (2000)
3. K U R A T O M I, S., ONO, K., M A T S U O K A, S., SARAI, N., NOMA, A.: Role of individual ionic current systems in ventricular cells hypothesized by a model study. Japanese Journal of Physiology 53, 105–123 (2003)
4. HELDT, T., SHIM, E.B., KAMM, R.D., MARK, R.G.: Computational modeling of cardiovascular response to orthostatic stress. Journal of Applied Physiology 92, 1239–1254 (2002)
5. Regen, D.: Calculation of left ventricular wall stress. Circ. Res. 67, 245–252 (1990)
6. JEW, B., DEWIT, B.: A physical approach to hemodynamic aspects of the human cardiovascular system. In: Reeve, EB., Guyton, AC. (eds.) Physical bases of circulatory transport: regulation and exchange. Philadelphia: Saunders, pp. 1–45 (1967)
7. Pruitt, AW., Gersony, WM.: The cardiovascular system. In: Behrman RE, (ed.) Nelson textook of pediatrics. 14th ed. Philadelphia: Saunders, pp. 1125–1227 (1992)
8. Gregory, GA.: Monitoring during surgery. In: Gregory, GA. (ed.) Pediatric anesthesia. New York: Churchill Livingstone, pp 261 – 279, (1994)
9. Graham Jr., TP., Jarmakani, MM.: Evaluation of ventricular function in infants and children. Pediatr. Clin. North Am. 18, 1109–1132 (1971)
10. Hagan, R., Diaz, F., Horvath, S.: Plasma volume changes with movement to the upright position. J. Appl. Physiol. 45, 415 (1978)
11. Moss, A.J., Emmanouilides, G.C., Monset-Couchard, M.: Vascular Responses to Postural Changes in Normal, Newborn Infants. Pediatrics 42, 250–254 (1968)
12. Edner, A., Katz-Salamon, M., Lagercrantz, H., Milerad, J.: Heart rate response profiles during head upright tilt test in infants with apparent life thereatening events. Archives of Disease in Childhood 76, 27–30 (1997)

30th Annual International IEEE EMBS Conference
Vancouver, British Columbia, Canada, August 20-24, 2008

An Approximation Model of Myocardial Crossbridge for Weak Coupling Calculation of Left Ventricle Model and Circulation Model

Akira AMANO, Yasuhiro TAKADA, Jianyin LU, Takao SHIMAYOSHI, Tetsuya MATSUDA

Abstract— **It is necessary to use complicated myocardial cell model and heart model to evaluate the regional energy production and consumption which leads to the unrealistic computational time. In this research, a left ventricle (LV) simulation model was constructed which includes accurate myocardial cell model. In order to simulate the model in realistic time, we introduced an approximation model of the crossbridge model which can be calculated with weak coupling calculation. The LV model was combined with a circulation model to validate the proposed model by calculating the hemodynamics parameters and ventricular energetics indices. The ESPVR (End Systolic Pressure Volume Relation) showed linear relation, and also the PVA - ATP consumption relation showed linear relation which are widely known as the physiological characteristics of mammalian hearts. From these results, we can say that the model can be used as a model for physiological simulation experiments which are related to the ventricular energetics.**

I. Introduction

Since many heart diseases are considered to come from the lack of the balance between the energy (ATP) production and consumption, it is very important to evaluate energetics of heart. The computer simulation of heart model with an accurate cell model is expected to be a power tool for such research. However, the computational cost of such model becomes very high since the accurate left ventricle (LV) model constructed from the accurate myocardial cell model and the LV tissue model needs to be calculated by the strong coupling calculation due to their physiological characteristics.

In this research, we propose a LV simulation model which can be used to evaluate regional and global energy production and consumption. The model includes an accurate myocardial cell model. In order to simulate the model in realistic time, we introduced an approximation model of the crossbridge mechanics model which can be calculated by weak coupling calculation.

A circulation model was combined with the model to validate the hemodynamic characteristics of the proposed model by calculating the hemodynamics parameters and ventricular energetics indices. The ESPVR (End Systolic Pressure Volume Relation) showed linear relation and also the PVA - ATP consumption relation showed linear relation which are widely known as the physiological characteristics of mammalian hearts which were difficult to reproduce in previous heart simulation researches.

A. Amano, Y. Takada, J. Lu, T. Matsuda is with Graduate School of Informatics, Kyoto Univerisity, Kyoto, 606-8501, Japan (phone:+81-75-753-3373; fax:+81-75-753-3375; e-mail:amano@i.kyoto-u.ac.jp)

T. Shimayoshi is with ASTEM RI, Kyoto, 600-8813, Japan

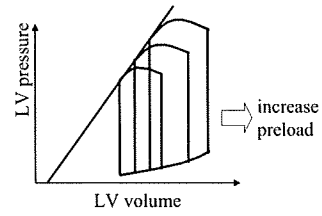

Fig. 1. Pressure volume loop under different preload.

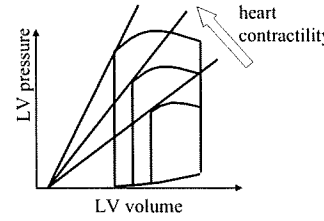

Fig. 2. Pressure volume loop under different heart contractility.

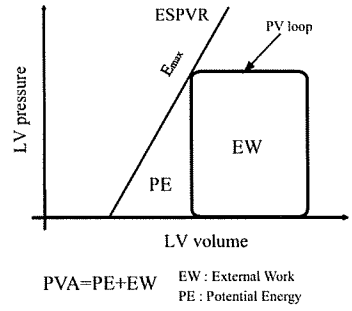

Fig. 3. PV Area (PVA)

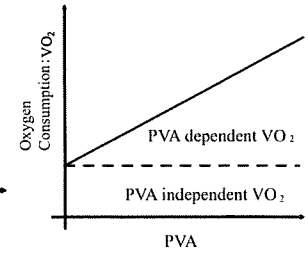

Fig. 4. PVA-VO_2 relation

II. Backgrounds

The pressure volume (PV) loop of LV are widely used to evaluate the heart performance which changes according to the afterload and the preload. The end diastolic pressure increases according to the increase of the preload which results in the increase of the stroke volume (Fig.1). The end systolic pressure increases according to the increase of the afterload which results in the decrease of the stroke volume.

Various PV loops can be obtained by providing various preloads and afterloads. It is widely known that the end systolic pressure volume points of LV distribute on a linear line [1]. This relation is called ESPVR (end-systolic pressure-volume relation) and the angle of this linear line is called E_{max} (maximum elastance). E_{max} is known to increase according to the increase in the heart contractility [1] (Fig.2). The physiological range of E_{max} of excised canine LV is reported to be 4.2 to 10.8[mmHg/ml] by Suga et al. [2]. Sunagawa et al. also reported that the canine E_{max} is 5.4 ± 1.00 [mmHg/ml] [3].

The closed loop area of a PV loop is called external work (EW) which corresponds to the external work of LV. Also the triangle area between an ESPVR and a PV loop is called potential energy (PE). The pressure volume area (PVA) is defined as the sum of EW and PE (Fig.3). PVA

978-1-4244-1815-2/08/$25.00 ©2008 IEEE.

TABLE I

LIST OF THE FUNDAMENTAL MODELS.

Element	Model	Species	Reference
cardiac cell	Kyoto model	guinea pig	[5]
left ventricle	Ring Shape	canine	[6]
tissue material	Mooney-Rivlin	canine	[7]
circulation	Nikos model	canine	[8]

is widely known to be linearly related to the ventricular oxygen consumption (VO_2) from many animal experiments [1] (Fig.4).

III. COUPLING CALCULATION OF LV MODEL AND CIRCULATION MODEL

A. Fundamental models

One of the most accurate myocardial cell model is Kyoto model [5] which is the only model which can calculate ATP consumption and production. Most of the physiological parameters are known to be related with body weight by a special function which is known as the allometric scaling [4]. Since the baseline RR interval of Kyoto model is 400[msec] which is close to the canine RR interval, it is natural to think that the physiological properties of Kyoto model is close to those of canine ones. Therefore, we used Kyoto model as canine cardiac cell model. The fundamental models of the proposed LV model are described in Table I.

B. Calculation scheme of the model.

The contraction model proposed by Negroni and Lascano (NL model) [9] is incorporated in Kyoto model. By denoting the concentration of the crossbridge states that develop force by [TCa*] and [T*], the contraction force F_b is represented by the following equation.

$$F_b = A(L - X)([TCa^*] + [T^*]) \tag{1}$$

Note that $A(= 1800[\mathrm{mN/mm^2}/\mu\mathrm{m}/\mu\mathrm{M}])$ is a constant which represents crossbridge spring constant. L represents half sarcomere length. The term $L - X$ represents the crossbridge elongation where X shortens according to the following equation.

$$dX/dt = B(L - X - h_c) \tag{2}$$

Note that B (=1.2[1/msec]) is a constant which represents crossbridge sliding rate. h_c is a constant.

Parallel elastic component of NL model is represented as follows.

$$F_{p,NL} = K_p(L_0 - L)^5 \tag{3}$$

In the physiological range, this equation can be approximated by the linear elastic component which can easily be modeled by many finite element solvers. Therefore, we used linear elasticity for the parallel elastic component which can be represented as follows.

$$F_p = K_l(L_0 - L) \tag{4}$$

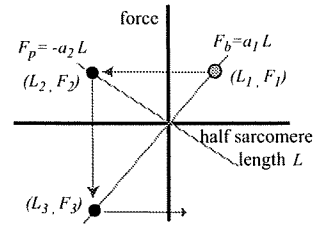

Fig. 5. Resulting sarcomere length and crossbridge force under weak coupling calculation.

Finally, from the following balance equation, we can calculate the sarcomere length i.e. tissue strain.

$$F_b = F_p + F_{ext} \tag{5}$$

Here, the term F_{ext} represents LV tissue stress which is related with LV blood pressure.

There are two types of calculation method in the coupling simulation: one is the strong coupling calculation, and the other is the weak coupling calculation. The strong coupling calculation gives accurate results however, the calculation time becomes large especially in the case of calculating complex simulation model. On the other hand, the calculation time becomes small for weak coupling calculation, however the accuracy of the result becomes low and in some case unstable.

In our model, the calculation step of these two methods can be described as follows.

strong coupling calculation:

$$\begin{aligned} &A(L^{(t_n)} - X^{(t_n)})([TCa^*]^{(t_n)} + [T^*]^{(t_n)}) = \\ &K_l(L_0 - L^{(t_n)}) + F_{ext}^{(t_n)} \end{aligned} \tag{6}$$

weak coupling calculation:

First, calculate contraction force from sarcomere length at time t_{n-1}.

$$F_b^{(t_n)} = A(L^{(t_{n-1})} - X^{(t_n)})([TCa^*]^{(t_n)} + [T^*]^{(t_n)}) \tag{7}$$

Then, calculate sarcomere length at time t_n.

$$F_b^{(t_n)} = K_l(L_0 - L^{(t_n)}) + F_{ext}^{(t_n)} \tag{8}$$

In the coupling calculation of a LV model and a circulation model, the weak coupling calculation is known to become unstable in some case. Therefore, strong coupling calculation is used in most case.

C. Condition of unstable calculation

Here, the condition of the unstability in the weak coupling calculation of NL model and the LV model is analyzed. For the simplicity, we only consider NL model and the LV mechanical model in this analysis.

The contraction force of NL model is described by equation (1) and the tissue passive force is described by equation (4). By denoting $a_1 = A([TCa^*] + [T^*])(a_1 > 0)$ and $a_2 = K_l(a_2 > 0)$, both forces can be denoted as follows.

$$F_b = a_1 L,\ F_p = -a_2 L \tag{9}$$

Here we assume that the half sarcomere length and the contraction force at time $t = 1$ be denoted as L_1, F_1. In the weak coupling calculation, the half sarcomere length at time $t = 2$ (L_2) is calculated from F_1 and the equation $F_p = -a_2 L_2$. Using this length, the contraction force at time $t = 2$ (F_2) is calculated from equation $F_2 = a_1 L_2$. By iterating these steps, the track of the half sarcomere length and the contraction force becomes as in Fig.5.

$$\begin{aligned}(L_1, F_1) &= (L_1, a_1 L_1)\\ (L_2, F_2) &= (-a_1/a_2 L_1, a_1 L_1)\\ (L_3, F_3) &= (-a_1/a_2 L_1, -a_1^2 L_1)\\ &\vdots\\ (L_n, F_n) &= \begin{cases} ((-a_1/a_2)^{n-1} L_1, (-a_1/a_2)^{n-1} a_1 L_1) \\ \qquad\qquad (n : odd) \\ ((-a_1/a_2)^{n} L_1, (-a_1/a_2)^{n-1} a_1 L_1) \\ \qquad\qquad (n : even) \end{cases}\end{aligned} \tag{10}$$

From this result, we can find that the weak coupling calculation becomes unstable if $\frac{a_1}{a_2} > 1 \Leftrightarrow a_1 > a_2$ which means that if the contraction force becomes larger than the tissue passive force, the calculation becomes unstable.

IV. Stable weak coupling calculation by the crossbridge approximation model

A. Approximation model

The weak coupling calculation is effective for reducing the computational time, however, the accuracy of the calculation results become low and in the myocardial cell and LV tissue coupling, the calculation becomes unstable. To overcome this problem, we propose a crossbridge approximation model.

In the force calculation equation (equation (1)), X changes according to equation (2). From these equations, X can be recognized as the first order delay variable of L. Note that by denoting the input signal as e, output signal as y, Laplace transformed variables of e and y as $E(s)$ and $Y(s)$, the first order delay system can be denoted as follows.

$$G(s) = Y(s)/E(s) = K\frac{1}{1+Ts} \tag{11}$$

Here, K is called the gain, T is called the time constant. By the inverse Laplace transformation, equation (11) is transformed into following equation.

$$y + T\frac{dy}{dt} = Ke \Leftrightarrow \frac{dy}{dt} = \frac{Ke - y}{T} \tag{12}$$

If we consider $e = L - h_c$, $y = X$, $K = 1$ and $T = 1/B$, then equation (2) becomes equivalent to equation (12).

Since this first order delay system is stable in weak calculation, we construct a crossbridge approximation model with this formulation. Here we replace $L - X$ in equation (1) by the constant h_c, and the number of crossbridge is calculated by the following first order delay system.

$$F_b = A \cdot h_c \cdot y \tag{13}$$

Here, y satisfies the following equation.

$$\frac{dy}{dt} = \frac{[TCa^*] + [T^*] - y}{T} \tag{14}$$

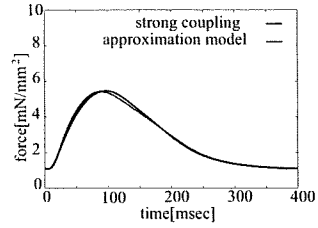

Fig. 6. Isotonic (noload) contraction.

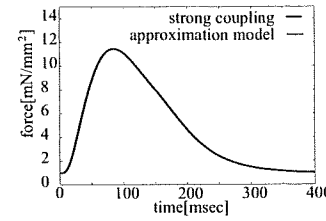

Fig. 7. Isometric contraction.

In the case of the isometric (fixed cell length) condition, the sarcomere length is fixed (L = const). In this case, the developed force is proportional to the number of crossbridge that means there is no delay in contraction force compared to the number of crossbridge.

To reproduce above characteristics, the time constant T is defined to be proportional to the sarcomere length change as follows.

$$T = \alpha|dL/dt| + \beta \tag{15}$$

Note that β was set to a small number compared to the maximum value of $\alpha|dL/dt|$.

B. Experimental results of the approximation model

Resulting developed force of the isotonic (free contraction) and the isometric condition with the strong coupling and the weak coupling with the proposed approximation model are presented in Fig.6 and Fig.7, respectively. The difference in the resulting total ATP consumption of both models were less than 1 %. From these results, we can say that the accuracy of the weak coupling calculation result for the approximation model is very high.

V. Experimental results

Pressure volume loop and the ATP consumption were evaluated for the proposed model by providing different preload and afterload values.

We used a ring shaped finite element model for the LV model which has 80 elements in the circumferential direction and 5 layers in the transmural direction. The myocardial cells are aligned with the circumferential direction. The LV volume was assumed to be proportional to the inner area of the ring where the end-diastolic volume was set to be 54[ml] according to the physiological value [6]. We used the Mooney-Rivlin material for the tissue where the corresponding Young's modulus was set to be 50[kPa]. The distribution of the cellular excitation time was determined by calculating the excitation propagation model with the same LV model.

The aortic compliance (C) was set to 0.25[ml/mmHg], and the characteristic impedance (R) was set to 2000, 3000, 4000 [mmHg·msec/ml] according to the published physiological values [8]. The preload (E_v) was set to 4.0, 7.0, 10.0[mmHg] according to the published physiological values [10]. 10 heart cycles were calculated with the model and the result of the last cycle was evaluated. The calculation time step